Crystal-field approach to rare-earth higher borides: Dimerization, thermal, and magnetic properties of RB_{50} (R = Tb, Dy, Ho, Er, Tm)

B. Z. Malkin,[1] S. L. Bud'ko,[2] and V. V. Novikov[3,*]

[1]*Kazan Federal University, Kremlevskaya 18, 420008 Kazan, Russia*

[2]*Ames Laboratory, U.S. DOE and Department of Physics and Astronomy, Iowa State University, Ames, Iowa 50011, USA*

[3]*Petrovsky Bryansk State University, Bezhitskaya 14, 241036 Bryansk, Russia*

(Received 6 January 2020; revised manuscript received 13 March 2020; accepted 9 April 2020; published 14 May 2020)

The microscopic justification for the dimerization in ladder-type rare-earth higher borides RB_{50} assumed by Mori [in *Handbook on the Physics and Chemistry of Rare Earths*, edited by K. A. Gschneidner, Jr., J.-C. G. Bünzli, and V. K. Pecharsky (North-Holland, Amsterdam, 2008), Vol. 38, p. 105] is presented. We consider a phenomenological model of crystal-field interactions and introduce Heisenberg antiferromagnetic exchange interactions between the rare-earth ions on the ladder rungs and the indirect exchange fields generated by magnetic interactions along the ladder legs. The crystal-field parameters and the exchange integrals for the rare-earth dimers are determined from modeling the temperature dependences of the heat capacity and static magnetic susceptibility. The field dependence of the low-temperature magnetization of polycrystalline samples of borides RB_{50} is simulated by making use of the proposed empirical expression for the renormalized magnetic moments of rare-earth ions. The characteristic anomalies of the thermal and magnetic properties of TbB_{50}, DyB_{50}, HoB_{50} and ErB_{50} are successfully reproduced within the framework of this approach.

DOI: 10.1103/PhysRevMaterials.4.054409

I. INTRODUCTION

Borides of rare-earth (RE) metals with a high boron content RB_{50} (R = Tb − Lu), as well as their pseudoisostructural analogs $RB_{44}Si_2$, crystallize in an orthorhombic structure with the space group *Pbam* [1]. This structure has several specific details. The unit cell of RB_{50} contains more than 330 atoms, and its volume V is rather large, in particular, $V = 2754.5$ Å^3 for LuB_{50} [2]. Rare-earth atoms are located inside cavities in a boron cluster's matrix, forming ladders which propagate, similarly to the B_{12} icosahedra chains along the c axis (see Fig. 1) [3]. The cavities containing the RE atoms have a peanut-type shape, and are not centrosymmetric. As a consequence, the RE atoms may occupy different closely spaced sites in the double-well cavity potential and form two-level centers in RB_{50} [2].

Measurements of specific heat and magnetic susceptibilities of RB_{50} borides [4–6] and isostructural rare-earth borosilicides $RB_{44}Si_2$ [7] revealed pronounced anomalies at low temperatures, which were assigned to transitions of the RE subsystem from the paramagnetic to the antiferromagnetic phase [4]. It is worth noting that the transition temperatures of these suggested phase transitions (from 4.6 K in ErB_{50} to 17.5 K in TbB_{50}) are unexpectedly rather high for magnetically dilute systems. The entropy increment with temperature appeared significantly less than $R \ln 2$. Neutron diffraction measurements [8] did not reveal antiferromagnetic structures at temperatures below maxima of the magnetic susceptibilities. These specific features as well as the broadness of anomalies and the absence of any changes with the substitution of nonmagnetic ions for the magnetic ones, along with the one-dimensional characteristics of the electron paramagnetic resonance spectra of GdB_{50} [9], gave evidence of short-range antiferromagnetic correlations only in the magnetic subsystems of RB_{50} and isostructural $RB_{44}Si_2$ compounds [8]. Mori and co-workers assumed that the observed anomalies of the susceptibility temperature dependences and field dependences of the magnetization take their origin from the specific ladder structure of higher borides where the alternative distances between the rungs are significantly larger than the rung length that leads to the formation of strongly coupled RE dimers [3,8,9]. However, this assumption has not been justified at a microscopic level [10,11].

Investigations of low-temperature thermal and magnetic properties of RE borides of different chemical compositions RB_x (x = 2, 4, 6, 50, 66) described in Refs. [3,12–16] revealed the remarkable influence of crystal fields affecting RE ions in these compounds on their physical characteristics. An analysis of the experimental data presented in Ref. [17] has shown that the observed anomalies of the heat capacity, thermal expansion, magnetic susceptibility, and magnetization of YbB_{50} can be successfully described within the corresponding crystal-field model. The study of the specific heat temperature dependence in the temperature range from 0.6 K up to room temperature, as well as of the low-temperature magnetic properties of YbB_{50}, did not reveal any anomalies which might be correlated with the magnetic ordering or the spin-glass state.

*Corresponding author: vvnovikov@mail.ru

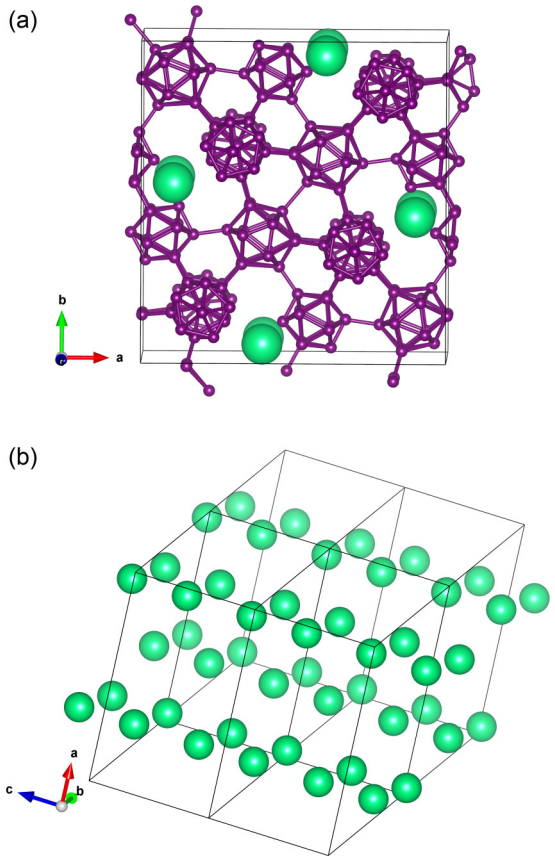

FIG. 1. (a) The fragment of crystal structure of RB_{50} borides. The small circles indicate boron atoms, while the large circles indicate RE atoms. (b) Ladders of RE atoms: The length of the rungs (0.386 nm) is less than the alternating distances between neighboring rungs (0.443 and 0.502 nm) along the c axis.

The main goal of the present study is to uncover the nature of the specific temperature dependences of the thermal and magnetic properties of RE borides RB_{50} at low temperatures by making use of a phenomenological crystal-field model in the analysis of the specific heat, the low-temperature magnetization, and the magnetic susceptibility of higher borides.

II. EXPERIMENTS AND EXPERIMENTAL RESULTS

The samples of RB_{50} (R = Tb, Dy, Ho, Er, Tm) were synthesized by the boron thermal reduction of RE elements from their oxides in vacuum. Details of the synthesis were described in Refs. [12–16]. The composition and homogeneity of the synthesized samples were controlled by x-ray phase, chemical, and spectral analysis. The lattice parameters at room temperature for the synthesized samples are presented in Table I. Small deviations of changes of the lattice parameters along the series Tb-Dy-Ho-Er-Tm-Lu from the expected monotonic decrease of a, b, and c due to the well-known lanthanide contraction, noted also in Ref. [4], are likely induced by the differences in the sample composition from the RB_{50} stoichiometry [1].

Magnetic susceptibilities $\chi(T) = M(B, T)/B$ in the 1.8–300 K temperature range were measured using a Quantum Design magnetic property measurement system superconducting quantum interference device (MPMS SQUID) magnetometer with an external magnetic field B of 0.1 T applied. Field-dependent magnetization $M(B,T)$ along the field B up to 7 T was measured at 1.8 and 300 K.

TABLE I. Lattice constants (nm) of the synthesized samples.

	LuB_{50}	TmB_{50}	ErB_{50}	HoB_{50}	DyB_{50}	TbB_{50}
a	1.6632	1.6597	1.6534	1.6608	1.6583	1.6598
b	1.7593	1.7606	1.7589	1.7614	1.7598	1.7603
c	0.9413	0.9469	0.9425	0.9459	0.9445	0.9466

The measured temperature dependences of the magnetic susceptibility and the field dependences of the magnetization of the borides studied in the present work are presented in Figs. 2–6. At elevated temperatures ($T > 100$ K), the inverse magnetic susceptibilities versus temperature (not shown) are successfully approximated by straight lines in accordance with the generalized Curie-Weiss (CW) law,

$$\chi(T) = \chi_0 + C/(T - \Theta), \quad (1)$$

where χ_0 is the temperature-independent magnetic susceptibility, $C = N_A\mu_{eff}^2/3k_B$ is the Curie constant (k_B is the Boltzmann constant, N_A is the Avogadro's number, and μ_{eff} is the effective magnetic moment of an ion), and Θ is the Curie temperature. The values of parameters χ_0, μ_{eff}, and Θ obtained from the fitting of the measurement data on the basis of Eq. (1) are presented in Table II. As seen in Table II, the effective magnetic moments are close to the magnetic moments of the corresponding free trivalent RE ions $\mu_{FI} = g_J[J(J+1)]^{1/2}\mu_B$ (here, g_J is the Landé factor of the ground multiplet with the total angular momentum J, and μ_B is the Bohr magneton). The obtained parameters describing the high-temperature susceptibilities agree satisfactorily with the literature data [4]. The effective magnetic moments evaluated from the $\chi(T)$ high-temperature tails are close to theoretical values for free

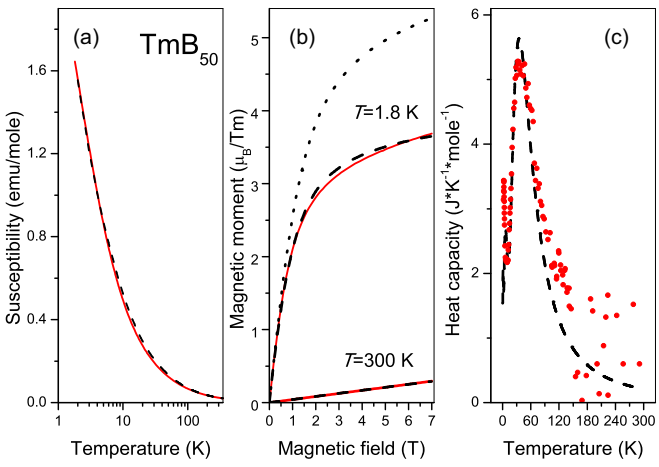

FIG. 2. Measured [solid red lines (the present work) and symbols [14]] and calculated (dashed lines) (a) magnetic susceptibility, (b) magnetic field dependences of the magnetization at the temperatures 1.8 and 300 K (the dotted line corresponds to the calculated powder-averaged single-ion magnetic moment M_{Av}), and (c) contributions of the Tm subsystem to the heat capacity of TmB_{50}.

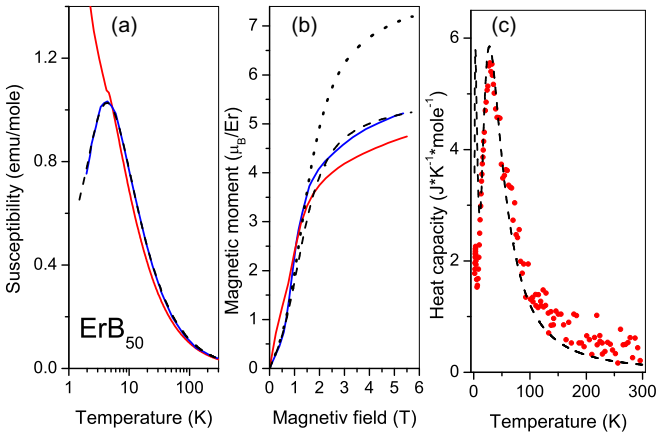

FIG. 3. Measured [solid blue [4] and red (the present work) lines and symbols [13]] and calculated (dashed lines) (a) magnetic susceptibility, (b) field dependences of the magnetization at $T = 1.8$ K [the dotted line represents the calculated powder-averaged magnetization of a single $(Er^{3+})_2$ dimer in the crystal and magnetic fields], and (c) contributions of the Er subsystem to the heat capacity of ErB_{50}.

R^{3+} ions. For all studied polycrystalline samples of RE higher borides, the Curie temperatures have a negative sign pointing to the dominant antiferromagnetic interactions between RE ions. Decreasing along the RE series from terbium to erbium, the absolute values of the Curie temperature correlate with the de Gennes factor $(1 - g_J)^2 J(J + 1)$ for RE ions coupled through the conduction electrons [7].

The quasilinear temperature dependence of the inverse susceptibility of TmB_{50} is observed down to the lowest temperature of 1.8 K (there are twelve $4f$ electrons localized at the Tm^{3+} ions). Similar behavior of the $1/\chi(T)$ curve was observed in Ref. [7] for the isostructural thulium borosilicide $TmB_{44}Si_2$.

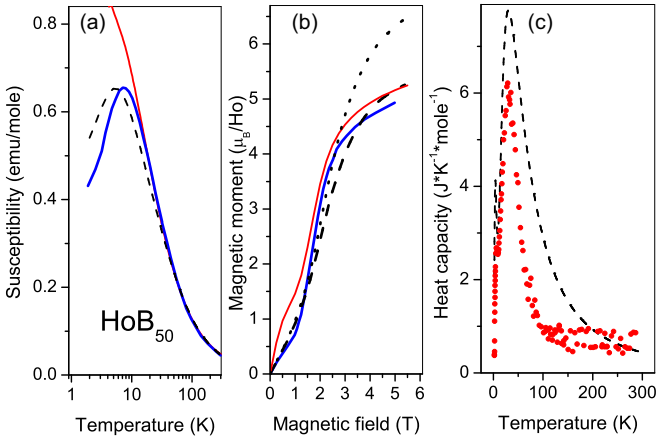

FIG. 4. (a) Temperature dependences of the magnetic susceptibility, (b) the magnetic field dependences of the magnetization, and (c) contributions of the Ho subsystem to the heat capacity of HoB_{50}. The experimental data are represented by symbols [16], blue [4] and red (the present work) solid lines, dashed lines correspond to the results of simulations, and the dotted line shows the calculated magnetic moment of Ho^{3+} ions for a single dimer in the crystal and magnetic fields.

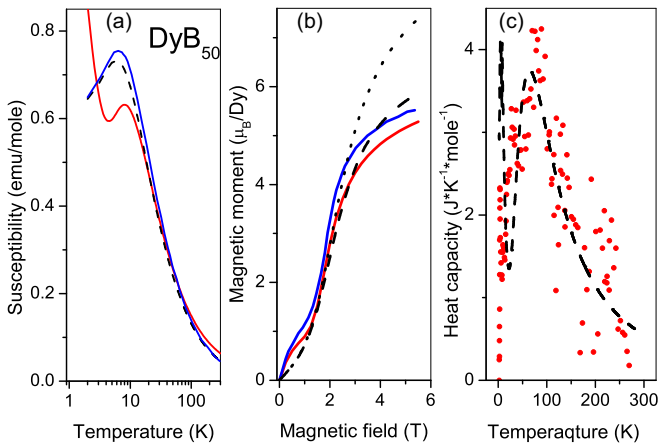

FIG. 5. Measured [solid blue [4] and red (the present work) lines and symbols [15]] and calculated (dashed lines) (a) magnetic susceptibility, (b) the field-dependent magnetization at $T = 1.8$ K [the dotted line shows the calculated magnetic moments for a single $(Dy^{3+})_2$ dimer in the crystal and magnetic fields], and (c) the contributions of the Dy subsystem to the heat capacity of DyB_{50}.

However, more complex behavior of the magnetic susceptibilities of other borides containing RE ions with less filled $4f$ electronic shells is observed. In particular, the susceptibility of the DyB_{50} sample has a broad maximum at the temperature $T_M = 8.1$ K (slightly larger than $T_M = 6.2$ K reported in Ref. [4]), but a sharp upturn appears with a further decrease in temperature, indicating a dominating paramagnetic contribution [Fig. 5(a)]. Similar maxima in the magnetic susceptibilities of TbB_{50}, HoB_{50}, and ErB_{50} at temperatures T_M presented in Table II were observed in Ref. [4], but these specific features of the low-temperature susceptibilities are hidden in the curves measured in the present work. Our measurements reveal only pronounced changes of the slopes $d\chi/dT$ at temperatures close to T_M and strong increases of the susceptibilities of TbB_{50}, HoB_{50}, and ErB_{50} at lower

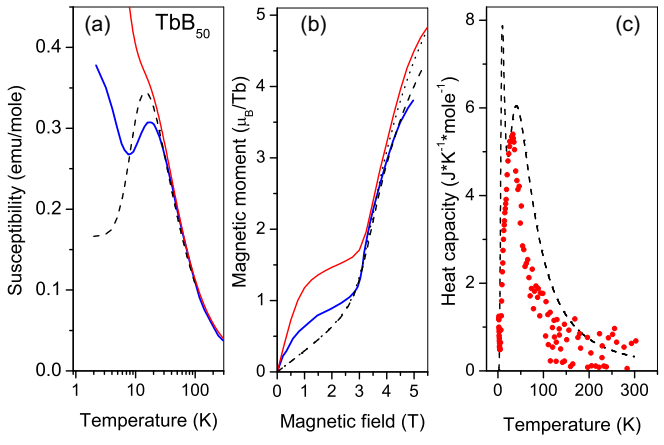

FIG. 6. Measured [symbols [12], solid blue [4] and red (the present work) lines] and calculated (dashed lines) (a) magnetic susceptibility, (b) the magnetic field dependence of the magnetization at $T = 1.8$ K [the dotted line shows calculated magnetic moments for a single $(Tb^{3+})_2$ dimer in the crystal and magnetic fields], and (c) the contributions of the Tb subsystem to the specific heat of TbB_{50}.

TABLE II. Parameters of the magnetic susceptibility [see Eq. (1)], temperatures T_M of the susceptibility maximum, magnetic fields H_C for the magnetization upturn, and exchange integrals for RE dimers (in degrees Kelvin). The effective ($\mu_{\rm eff}$) and free ion ($\mu_{\rm FI}$) magnetic moments are in units of the Bohr magneton.

Compound	χ_0 (emu/mol)	$\mu_{\rm eff}/\mu_{\rm FI}$	Θ (K)	T_M (K)	H_C (T)	$J_{\rm eff}$ (K)	κ (μ_B^{-1})
TbB_{50}	0	9.95/9.72	−13.0		2.92	−0.565	0.020
	−0.007[a]	10.3/9.72[a]	−15.3[a]	17.5[a]	3.0[a]		
DyB_{50}	0.015	11.0/10.65	−13.2	8.1	1.76	−0.330	0.035
		11.9/10.65[a]	−13.7[a]	6.2[a]	1.8[a]		
HoB_{50}	0.003	10.4/10.61	−8.10		1.65	−0.248	0.035
		11.5/10.61[a]	−13.7[a]	7.5[a]	1.6[a]		
ErB_{50}	0.002	8.9/9.58	−4.70		0.95	−0.120	0.052
		9.74/9.58[a]	−5.4[a]	4.6[a]	0.8[a]		
TmB_{50}	0	7.61/7.56	−8.2				0.084

[a]From Ref. [4].

temperatures. The differences between our and the literature data are due partly to different magnetic fields used in the measurements, namely, of 0.1 T in the present work instead of 1 T for TbB_{50}, HoB_{50}, and DyB_{50}, and 0.5 T for ErB_{50} in Ref. [4].

The magnetic field dependences of the magnetization of TmB_{50} exhibit no features in the range of available temperatures [Fig. 2(b)]. Of note is the absence of saturation even at the base temperature of 1.8 K in strong magnetic fields up to 7 T. However, a steplike behavior of $M(B)$ curves at a temperature of 1.8 K, similar to that reported in Ref. [4], is observed for borides containing RE ions with fewer electrons in the $4f$ shell. The most pronounced upturn of the field-dependent magnetization with the increase of the external magnetic field appears in the field $H_C = 3$ T for TbB_{50} [Fig. 6(b)]. Similar but weaker features are observed at lower fields H_C corresponding to the maxima in dM/dB (see Table II) for DyB_{50}, HoB_{50}, and ErB_{50} [Figs. 5(b), 4(b), and 3(b)].

As follows from a comparison of the low-temperature magnetic susceptibility and magnetization measured in the present work and those published earlier in Ref. [4], the magnetic properties of borides RB_{50} are strongly sample dependent. Differences between the slopes of the magnetization curves in weak magnetic fields give evidence of different concentrations of paramagnetic defects in the polycrystalline RE borides studied in Ref. [4] and in our samples. The maxima in the temperature dependences of the magnetic susceptibility at low temperatures observed in Ref. [4] for TbB_{50}, ErB_{50}, and HoB_{50} can be connected with antiferromagnetic correlations of magnetic moments. However, this effect is hidden by the contribution from paramagnetic defects, presumably of RE single-ion type, in the samples studied in the present work. Rather large concentrations of defects also cause differences in the field dependences of the low-temperature magnetization in the range of weak magnetic fields where the nonlinear increase of the magnetic moments of RE ions is observed instead of the quasilinear behavior of the dimer magnetization that is considered below.

III. THEORETICAL AND EMPIRICAL MODELING

A. Single-ion approximation

The following Hamiltonian operating in the space of states of the ground multiplet with the total angular momentum J of a RE ion is considered in the present work,

$$H = H_{\rm CF} + H_Z. \tag{2}$$

Here, $H_{\rm CF}$ corresponds to the interaction of $4f$ electrons with the static crystal lattice, and H_Z is the Zeeman interaction with the local magnetic field. The observation of magnetic moments with values of several Bohr magnetons for non-Kramers RE ions in polycrystalline low-symmetry samples gives evidence for relatively weak low-symmetry components of the crystal fields (CFs). We write the CF Hamiltonian in the following form,

$$H_{\rm CF} = B_4\left(O_4^0 + 5O_4^4\right) + B_6\left(O_6^0 - 21O_6^4\right) + \sum_{pk} B_p^k O_p^k, \tag{3}$$

where O_p^k are the Stevens operators including the corresponding reduced matrix elements [18] and B_p, B_p^k are the CF parameters. The CF parameters are determined below from the analysis of the experimental data. Accounting for the high density of boron atoms in the unit cell, we identify (following Ref. [17]) the dominant cubic CF component defined by the parameters B_4 and B_6. Additional relatively weak low-symmetry CF components are defined by the parameters B_p^k. Because of the low symmetry at the RE sites, we are not able to connect the considered coordinate frame with the crystallographic system of coordinates. The direction of the local magnetic field $\boldsymbol{B}_{\rm loc}$ is defined by the spherical angles θ and φ. Following the mean-field approximation (MFA), we determine the local field as

$$\boldsymbol{B}_{\rm loc} = \boldsymbol{B} + \boldsymbol{\lambda M}, \tag{4}$$

where $\boldsymbol{B}$ is the external field, $\boldsymbol{M}(\boldsymbol{B})$ is the equilibrium magnetic moment of the considered RE ion, and $\boldsymbol{\lambda}$ is a molecular field tenor. The Zeeman energy of the $4f$ electrons takes the form

$$H_Z = g_J\mu_B(J_x\cos\varphi\sin\theta + J_y\sin\varphi\sin\theta + J_z\cos\theta)B_{\rm loc}. \tag{5}$$

In accordance with the definition, the magnetic moment of a RE ion is determined by the expression $\boldsymbol{M}(\boldsymbol{B}) = -\langle g_J\mu_B\boldsymbol{J}\rangle$, where the angular brackets mean quantum-statistical averaging, $\langle A\rangle = {\rm Tr}[A\exp(-H/k_BT)]/{\rm Tr}[\exp(-H/k_BT)]$. Thus, we obtain a self-consistent equation for the magnetic moment

TABLE III. Crystal-field parameters B_p^k (cm^{-1}) for RB_{50} borides obtained from fittings of the magnetic susceptibility and heat capacity data.

p	k	R = Tb	R = Dy	R = Ho	R = Er	R = Tm
4		−45	−45	−34	−37.2	−17
6		−26	−14.5	−10.2	−2.2	−6.9
2	0	−15	−22	−21	−9	−3
2	2	−14	−14	−12	−8	−5
4	4	−25	−10	0	−5	−3
6	4	4	−5	−20	0	3
4	2	−30	−25	−28	−20	−5
6	2	15	18	15	5	5
6	6	5	25	25	8	2

in the fixed local field $\boldsymbol{B}_{\rm loc}$,

$$\boldsymbol{M} = -g_J\mu_B \frac{\mathrm{Tr}\{\boldsymbol{J}\exp\left[-(H_{\rm CF}+H_{\rm Z})/k_{\rm B}T\right]\}}{\mathrm{Tr}\{\exp[-(H_{\rm CF}+H_{\rm Z})/k_{\rm B}T]\}}. \quad (6)$$

The magnetic moment dependence on the external field $\boldsymbol{M}(\boldsymbol{B})$ can be obtained numerically for a fixed temperature T from Eq. (4), where the nonlinear function $\boldsymbol{B}_{\rm loc}(\boldsymbol{M})$ stands for the inverse function (6) $\boldsymbol{M}(\boldsymbol{B}_{\rm loc})$. For simplicity, neglecting magnetic dipole-dipole interactions and the anisotropic terms of the exchange interactions between the RE ions, we consider the molecular field tensor in Eq. (4) as a scalar quantity. For polycrystalline samples, the average values of the magnetic moments were calculated numerically by making use of the integral over the projections of magnetic moments on the external magnetic field $\boldsymbol{B}$ for a set of spherical angles [see Eq. (5)] uniformly distributed over a sphere using steps of $\Delta\theta = \pi/20$ and $\Delta\varphi = \pi/15$,

$$M_{\rm Av}(B,T) = \frac{1}{4\pi}\int M(\boldsymbol{B},T)\sin(\theta)d\theta d\varphi. \quad (7)$$

The fitting procedure for the susceptibility and magnetization curves involved simultaneous calculations of the heat capacity of the RE subsystem to account for the actual scale of the CF energies,

$$C_R(T) = \frac{N_{\rm A}}{k_{\rm B}T^2}[\langle H^2\rangle - \langle H\rangle^2]. \quad (8)$$

The temperature dependences of the heat capacity for different higher borides RB_{50} were measured earlier in Refs. [12–16].

The CF parameters and the corresponding CF energies of Tm^{3+} ions in TmB_{50} obtained from the analysis of the experimental data are presented in Tables III and IV, respectively.

Three lower CF levels originate from the Γ_5 triplet in the cubic CF component with the effective g-factor $g \sim 6$. The single-ion approach considered above allowed us to describe satisfactorily the temperature dependences of the magnetic susceptibility and the heat capacity neglecting magnetic interactions between the Tm^{3+} ions [Figs. 2(a) and 2(c)]. However, this approximation leads to significantly overestimated (up to 30%) magnetic moments of Tm^{3+} ions at low temperatures in strong magnetic fields [see the dotted line in Fig. 2(b)]. The measured magnetization can be reproduced in the framework of MFA but only with the field-dependent parameter λ (increasing approximately linear with the applied field B) in

TABLE IV. Calculated crystal-field energies (cm^{-1}) of the ground multiplet sublevels for R^{3+} ions in RB_{50}.

Tb^{3+} ($^7F_6$)	Dy^{3+} ($^6H_{15/2}$)	Ho^{3+} ($^5I_8$)	Er^{3+} ($^4I_{15/2}$)	Tm^{3+} ($^3H_6$)
0	0	0	0	0
1.45	3.11	0.15	2.23	0.16
11.3	4.83	2.88	10.1	1.79
12.9	10.4	25.4	48.1	9.03
17.3	101.8	37.4	49.3	13.2
75.2	108.0	47.5	59.2	62.5
78.5	121.4	58.1	60.4	62.7
82.2	125.7	58.3	64.8	64.4
82.3		64.1		70.1
92.3		64.6		70.3
93.1		67.5		70.4
95.2		85.0		70.7
104.7		128.9		86.1
		136.6		
		136.7		
		139.5		
		144.4		

Eq. (4) that can be connected with the increasing polarization of the charge carriers. We found it possible to significantly simplify the simulation procedure by introducing the renormalized powder-averaged magnetization

$$M(B,T) = M_{\rm Av}(B,T)[1+\kappa M_{\rm Av}(B,T)]^{-1}, \quad (9)$$

where the factor κ was considered as the fitting parameter.

The semiempirical expression (9) is qualitatively consistent with the linear dependence of the mean-field parameter λ on the field B. For $\kappa = 0.0864\ \mu_B^{-1}$, we obtained the field dependences of the magnetization of TmB_{50} [the dashed curves in Fig. 2(b)] that match well the measurement data in the total magnetic field range from 0 to 7 T at temperatures 1.8 and 300 K.

We found it impossible to reproduce the observed nonmonotonic variations of the magnetic susceptibility with temperature and the sharp rise of magnetic moments in the increasing external magnetic fields in the RE borides TbB_{50}, DyB_{50}, HoB_{50}, and ErB_{50} in the framework of the single-site MFA [Eq. (4)]. Remembering the main structure motif of higher borides, i.e., ladders with alternative bonds, we turn to the next step of our analysis of the electronic structure of RE ions to the nearest-neighbor pairs of RE ions forming the rungs of the ladders.

B. Rare-earth dimers

The Hamiltonian of a RE dimer is written in the form

$$H_{\rm dim} = H_1 + H_2 - J_{\rm eff}\boldsymbol{J}_1\cdot\boldsymbol{J}_2, \quad (10)$$

where $H_i (i = 1, 2)$ and $\boldsymbol{J}_i$ are the single-ion Hamiltonian (2) and the angular momentum operator, respectively, and the last term on the right-hand side of Eq. (10) is the isotropic exchange interaction. The local magnetic field $\boldsymbol{B}_{\rm loc} = \boldsymbol{B} + \lambda_d\boldsymbol{M}$ affecting the ions in a dimer is determined now by the

molecular field constant λ_d that corresponds to interdimer interactions along the ladder legs.

The expression for the average magnetic moment of an ion in a single dimer along the external field $\boldsymbol{B}$ takes the form

$$M_d(\boldsymbol{B}, T) = -g_J \mu_B \tfrac{1}{2} \mathrm{Tr}[(\boldsymbol{J}_1 + \boldsymbol{J}_2) \cdot \boldsymbol{B} \rho(\boldsymbol{B}, T)]/B, \quad (11)$$

where

$$\rho(\boldsymbol{B}, T) = \exp(-H_{\mathrm{dim}}/k_{\mathrm{B}}T)/\mathrm{Tr}[\exp(-H_{\mathrm{dim}}/k_{\mathrm{B}}T)] \quad (12)$$

is the corresponding equilibrium density matrix. The powder averaging is performed in accordance with Eq. (7). The heat capacity of the RE dimer subsystem can be calculated using the expression

$$C_R(T) = \frac{N_{\mathrm{A}}}{2k_{\mathrm{B}}T^2}\left[\langle H_{\mathrm{dim}}^2\rangle - \langle H_{\mathrm{dim}}\rangle^2\right]. \quad (13)$$

The results of simulations of the temperature dependences of the heat capacity and magnetic susceptibility and the calculated magnetic field dependences of the magnetic moments of the RE ions at the temperature 2 K in the borides DyB_{50}, HoB_{50}, ErB_{50}, and TbB_{50} in the framework of a dimer model are compared with the measurement data in Figs. 3–6. The CF parameters obtained from the fitting procedures and the corresponding CF energies are presented in Tables III and IV, respectively, and the effective exchange integrals J_{eff} for dimers of different compositions can be compared in Table II. It is possible that narrow maxima in the simulated heat capacity curves at low temperatures [see Figs. 3(c), 5(c), and 6(c)] are significantly broadened by magnetic interactions and random strains in the studied higher borides ErB_{50}, DyB_{50}, and TbB_{50} [19]. We suppose that the measured magnetization curves in weak magnetic fields and the susceptibility curves at low temperatures contain remarkable contributions from the paramagnetic defects. The approximation of noninteracting dimers leads to a significant overestimation of the magnetic moments $M_{\mathrm{d,Av}}(B, T)$ calculated in accordance with Eqs. (11) and (7) for strong magnetic fields [$B > 2.5$ T; see the dotted lines in Figs. 3(b)–6(b)] as compared with the experimental data. The fitting procedure in the framework of the MFA leads again, similarly to the presented above analysis of the magnetization of TmB_{50}, to the field-dependent molecular field parameters λ_d. To account for the antiferromagnetic interactions between the RE ions belonging to the nearest-neighbor rungs in the ladders and the possible screening of RE ions by polarized charge carriers, we employed expression (9); the corresponding renormalization factors κ for the polycrystalline samples studied are presented in Table II.

The single-ion operator of the total spin moment is defined as $\boldsymbol{S}_i = (1 - g_J)\boldsymbol{J}_i$. Variations of the effective exchange integrals along the RE series, from Tb^{3+} to Er^{3+} ions (see Table II), correlate with the factor $(1 - g_J)^2 = 1/4(Tb^{3+})$, $1/9(Dy^{3+})$, $1/16$ (Ho^{3+}), and $1/25$ (Er^{3+}). Thus, we can assume that the value of J_{ex} in the generic form of the exchange Hamiltonian ($H_{\mathrm{ex}} = -J_{\mathrm{ex}}\boldsymbol{S}_1 \cdot \boldsymbol{S}_2$) is nearly constant. This explains why no signs of dimer-type magnetic correlations have been observed for the magnetic susceptibility and the low-temperature magnetization of TmB_{50} [$(1 - g_J)^2 = 1/36$] in the present work and YbB_{50} [$(1 - g_J)^2 = 1/49$] in Ref. [17].

IV. CONCLUSION

In the present work, we demonstrated the possibility of reproducing successfully the specific features of the temperature dependences of the heat capacity and dc-magnetic susceptibility, and the magnetic field dependence of the magnetization of high-molecular terbium, dysprosium, holmium, and erbium borides RB_{50} within the framework of the RE dimer model. Our analysis confirmed the existence of short-range magnetic correlations in the RE subsystems predicted earlier by Mori *et al.* [8,9] on the basis of the studies of neutron scattering, dilution effects, and electron paramagnetic resonance spectra. The temperatures T_M of the observed maxima of the dc-magnetic susceptibilities determine the strength of the exchange interaction in the RE dimers on the rungs of the ladders which are the main structural motif of the RE subsystem in higher borides and borosilicides [1]. Despite the low point symmetry at the positions of RE ions in the crystal lattice of higher borides, the CF component of cubic symmetry plays a dominant role in the formation of the spectra of CF excitations. Accordingly, one may suppose that the RE ions are coupled through the charge carriers. Understanding the mechanisms responsible for the formation of relatively weak crystal fields and exchange interactions in boron compounds containing paramagnetic ions remains a challenging problem.

ACKNOWLEDGMENT

The research was performed under the auspices of the Russian Science Foundation (Project No. 16-12-00004 P).

[1] I. Higashi, T. Tanaka, K. Kobayashi, Y. Ishizawa, and M. Takami, J. Solid State Chem. **133**, 11 (1997).
[2] V. V. Novikov, N. A. Zhemoedov, A. V. Matovnikov, N. V. Mitroshenkov, S. V. Kuznetsov, and S. L. Bud'ko, Dalton Trans. **44**, 15865 (2015).
[3] T. Mori, Higher borides, in *Handbook on the Physics and Chemistry of Rare Earths*, edited by K. A. Gschneidner, Jr., J.-C. G. Bünzli, and V. K. Pecharsky (North-Holland, Amsterdam, 2008), Vol. 38, p. 105.
[4] T. Mori and T. Tanaka, J. Phys. Soc. Jpn. **69**, 579 (2000).
[5] T. Mori, T. Tanaka, H. Kitazawa, H. Abe, N. Tsujii, and G. Kido, Physica B **312-313**, 870 (2002).
[6] T. Mori and T. Tanaka, J. Alloys Compd. **348**, 203 (2003).
[7] T. Mori, Z. Kristallogr. **221**, 464 (2006).
[8] T. Mori, F. Izumi, and Y. Ishii, J. Alloys Compd. **374**, 105 (2004).
[9] T. Mori, J. Appl. Phys. **99**, 08J309 (2006).
[10] T. Mori, J. Solid State Chem. **275**, 70 (2019).
[11] S. Gabani, K. Flachbart, K. Siemensmeyer, and T. Mori, J. Alloys Compd. **821**, 153201 (2020).

[12] V. V. Novikov, N. A. Zhemoedov, A. V. Matovnikov, N. V. Mitroshenkov, B. I. Kornev, S. V. Kuznetsov, E. A. Popova, B. G. Ueland, S. L Bud'ko, and A. K. Tolstosheev, J. Therm. Anal. Calorim. **129**, 15 (2017).

[13] V. V. Novikov, N. A. Zhemoedov, A. V. Matovnikov, N. V. Mitroshenkov, B. G. Ueland, and S. L. Bud'ko, J. Alloys Compd. **684**, 714 (2016).

[14] V. V. Novikov, N. A. Zhemoedov, N. V. Mitroshenkov, and A. V. Matovnikov, Dalton Trans. **45**, 17447 (2016).

[15] V. V. Novikov, N. A. Zhemoedov, A. V. Matovnikov, N. V. Mitroshenkov, S. V. Kuznetsov, and S. L. Bud'ko, J. Magn. Magn. Mater. **449**, 257 (2018).

[16] V. V. Novikov, N. A. Zhemoedov, A. V. Matovnikov, N. V. Mitroshenkov, S. V. Kuznetsov, and S. L. Bud'ko, J. Alloys Compd. **724**, 782 (2017).

[17] V. V. Novikov, N. A. Zhemoedov, A. V. Matovnikov, N. V. Mitroshenkov, E. A. Popova, A. K. Tolstosheev, B. Z. Malkin, and S. L. Bud'ko, Phys. Rev. Mater. **2**, 054401 (2018).

[18] A. Abragam and B. Bleaney, *Electron Paramagnetic Resonance of Transition Ions* (Clarendon Press, Oxford, UK, 1970).

[19] N. E. Sluchanko, A. L. Khoroshilov, A. V. Bogach, S. Yu. Gavrilkin, V. V. Glushkov, S. V. Demishev, V. N. Krasnorussky, N. Yu. Shitsevalova, V. B. Filipov, S. Gabani, K. Flachbart, and B. Z. Malkin, JETP Lett. **108**, 454 (2018).